A study on the effect of ultrashort pulsed laser texturing on the microstructure and properties of metastable S phase layer formed on AISI 316L surfaces

Dashtbozorg, Behnam; Li, Xiaoying; Romano, Jean-Michel; Garcia Giron, Antonio; Sammons, Rachel; Dimov, Stefan; Dong, Hanshan

Link to publication on Research at Birmingham portal

A Study on the Effect of Ultrashort Pulsed Laser Texturing on the Microstructure and Properties of Metastable S Phase Layer formed on AISI 316L Surfaces

Behnam Dashtbozorg[a]* (bxd126@bham.ac.uk), Xiaoying Li[a] (x.li.1@bham.ac.uk), Jean-Michel Romano[b] (jean-michel.romano@gadz.org), Antonio Garcia-Giron[b] (axg616@bham.ac.uk), Rachel L. Sammons[c] (r.l.sammons@bham.ac.uk), Stefan Dimov[b] (s.s.dimov@bham.ac.uk) and Hanshan Dong[a] (h.dong.20@bham.ac.uk)

[a]School of Metallurgy & Materials, University of Birmingham, Birmingham, B15 2SE, UK; [b]School of Mechanical Engineering, University of Birmingham, Birmingham, B15 2TT, UK; [c]School of Dentistry, University of Birmingham, Birmingham, B5 7EG, UK.

*Corresponding author. Telephone number: +44 (0)7988 188036. Email address: bxd126@bham.ac.uk

Abstract

Austenitic stainless steels (ASS) are an important material within the food and medical industries. However, their current limitations of poor wear resistance and susceptibility to bacterial colonisation have limited further uptake. Low-temperature plasma nitriding can address the poor durability of the ASS alloys by forming the S phase, therefore, providing combined improvement in hardness, wear resistance and corrosion resistance. Additionally, pulsed laser texturing can also be used to introduce functional antibacterial textures. However, due to the thermal nature of laser patterning and the thermodynamic metastability of the S phase, almost no research has been conducted thus far on combining the technologies.

Therefore, this study for the first time has investigated the response of S phase treated surfaces to ultrashort (nano and femtosecond) laser texturing. The results have shown that, both theoretically and in practice, laser pulses within the nanosecond regime led to the damage of the surface, decomposition of the metastable S phase and loss of the corrosion resistance. In contrast, no change of the S phase surface layer could be detected following femtosecond laser texturing. Hence, demonstrating the feasibility of texturing S phase surfaces using femtosecond pulsed lasers, thus paving the way towards long-lasting multi-functional antibacterial stainless steel surfaces.

1 Introduction

Austenitic stainless steels are one of the most important materials for the food and the medical industries [1]. Resulting from their superior corrosion resistance, bio-inertness and excellent formability, they have found widespread applications as medical scalpels, bone saws, surgical sutures, bone fixation pins, pressure vessels, storage containers, cutlery, cutting tools and piping [2-6]. Although austenitic stainless steels alloys are currently the materials of choice for these applications, there are still some serious concerns with their use. The largest worry is related to the high susceptibility of these surfaces to the attachment and growth of bacteria [4, 7, 8]. It is thought that this arises due to the high surface free energy (and hydrophilic nature) of the materials, which attracts bacteria in a liquid medium to the surface and then allows chemical and physical bonds to be made [9]. The other major concern is related to the relatively low hardness and poor wear resistance of the materials, which limits their longevity and requires regular maintenance [9-11]. These are obviously key issues within the food and medical industries as they lead to the contamination of foods, damage of equipment, food poisoning, infection of patients and, ultimately, death [12].

Two potential solutions to these issues are laser surface texturing and surface hardening. The idea of surface hardening is quite self-explanatory, by increasing the hardness at the surface it is possible to reduce the wear and damage that arises in service. Whereas, laser texturing can enable the modification of the surface free energy as well as the introduction or enhancement of properties such as anti-icing, colour, antimicrobial activity and cell biocompatibility of the surface [13-15]. However, many of the functional properties related to surface texturing depend on the existence of homogeneously spread micro- or nano-scale features, with very limited tolerance for damage [16, 17]. Therefore, given that untreated austenitic stainless steels possess poor resistance to wear and damage, such desirable functional properties are unlikely to be long-lasting [12, 18]. Thus, the ideal solution would be to combine surface hardening and surface texturing to produce durable functional surfaces. However, combination of the techniques without detrimental drawbacks has proven to be difficult [14].

Traditional surface hardening approaches (carried out between 500 and 1100 °C) include nitriding, carburising and nitrocarburising, which all help to harden the surface through the formation of hard precipitates (nitrides and carbides). Although this is effective in improving the wear resistance of these surfaces, it ultimately deprives the surface of free chromium necessary for forming the passive chromium oxide film [19, 20]. Hence, this leads to a rapid loss of corrosion resistance, which is extremely detrimental for food and medical applications, where corrosive solutions, bacteria and cells are present [21].

Since the early 1980's a new more promising approach to surface treatments has come about that involves the use of lower temperatures (typically around 400-450 °C) which enable the hardening of the stainless steel surface without loss of the corrosion resistance [10, 22]. The principle behind this type of hardening is that at lower temperatures interstitial elements (nitrogen and carbon) can still freely diffuse into the surface, but the activation energy required for substitutional elements (e.g. chromium) to move and react to form the stable precipitates is not readily achieved [20, 23]. Subsequently, the interstitial supersaturation

leads to effective solid solution hardening [10]. For the purposes of this paper, only nitriding will be discussed from this point on, although the details are similar for carburising and nitrocarburising.

Low-temperature surface nitriding has been shown to be effective for stainless steel and cobalt-chromium alloys. In the case of austenitic stainless steels, this type of treatment results in the formation of a precipitate-free surface layer that demonstrates high hardness (1000-1500 HV0.05) and marginally improved corrosion resistance over its untreated counterpart [3, 10, 24]. The surface layer has also been shown to contain nitrogen content reaching up to 22 atomic percent, which is much greater than the maximum nitrogen solid solubility in austenite (8.7 at%) [25-29].However, the greatest limitation of the S phase is that it is a thermodynamically metastable phase that will, upon heating, decompose into nitride precipitates and a chromium depleted austenite phase [26, 30].

The introduction of micro- or nano-scale features onto surfaces typically involves the addition or removal of material. The durability of functional surfaces achieved through material addition depends on the wear resistance of the material being added to the surface; which is counterintuitive on an already hardened (S Phase) surface. Additionally, material removal typically involves heating of a surface to re-organise or melt/ablate material from the surface [13, 31]. Given the metastable nature of the S phase, this poses a serious problem. A recent industrial report also discovered a similar issue (nitride precipitation) following the heating of low-temperature nitrocarburised AISI 316L stainless steel during laser welding [32]. The alternative solution would be to texture the surface prior to treatment, however, this leads to a rounding of the features (due to the sputtering mechanism) and at least some loss of properties [33].

Therefore, the challenge faced when attempting to combine surface texturing and low-temperature nitriding is how can desirable textures be produced on the thermodynamically metastable S phase without damage. Due to the above barriers, very little research has been carried out thus far on the surface functionalisation via texturing of S phase treated stainless steel surfaces. However, the recent development and increased availability of ultrashort nanosecond (10^{-9} s) and femtosecond (10^{-15} s) pulsed lasers could create new opportunities for the functionalisation of S phase surfaces [34]. However, no research has been published on the response of the metastable S phase to texturing using these ultrashort pulsed lasers.

Hence, this study for the first time examines the response of S phase treated austenitic stainless steel samples to ultrashort (nano and femtosecond) laser texturing using both experimental and simulation approaches. Scientifically, the outcomes should answer some fundamental and scientifically interesting questions regarding the stability and decomposition of the S phase under pulsed laser texturing. Technologically, this could identify a suitable laser texturing technology to pave the way towards long-lasting multi functionalised stainless steel surfaces, thus expanding their industrial applications.

2   Materials & Methods

2.1 Sample Preparation & Active Screen Plasma Nitriding

AISI 316L austenitic stainless steel (ASS) cylinders (25 mm x 5 mm) were initially ground to 1200 grit size and then polished using 6 µm, 3 µm and finally 1 µm diamond suspensions. Teepol and acetone ultrasonic cleaning was performed between each step.

Active screen plasma nitriding (ASPN) was carried out in an adapted DC Klöckner Ionon 40 kW plasma furnace. Freshly polished samples were treated for 20 hours at 400 °C in a gas pressure of 3 mbars and gas mixture of 25 % N_2: 75 % H_2. Samples were kept at a floating potential and enclosed in an AISI 316 ASS active screen and cage. A distance of 20mm was used to separate the surface of the samples and the screen. Following the treatment, samples were briefly polished with a 1 µm diamond suspension to remove loose deposits.

2.2 Laser Texturing

Four types of samples were formed following ASPN treatment (see Table 1): as-treated (As-treated), 310 femtosecond textured (310 fs), 15 nanosecond textured (15 ns) and 220 ns textured (220 ns). The as-treated samples were the re-polished samples directly after ASPN treatment. Channels with 300 µm spacing were formed on all of the textured samples. Both nanosecond textures were performed using a MOPA-based Yb-doped fibre on a SPI G4 50W HS-S set up with a laser source wavelength of 1064 nm. The femtosecond texturing was performed using a Satsuma from Amplitude Systemes fitted with a 1032 nm wavelength laser source. The theoretical amount of energy delivered to the surface per unit distance travelled was kept constant between all textures by altering the frequency and speed of the laser (moving energy density). The details of the laser settings are listed in Table 1.

Table 1 Pulsed laser texturing settings for all sample types.

Sample Code	As-treated	310 fs	15 ns	220 ns
Wavelength (nm)	-	1032	1064	1064
Gaussian spot radius (µm)	-	15	15	15
Pulse Duration (s)	-	3.1×10^{-13}	1.5×10^{-8}	2.2×10^{-7}
Frequency (kHz)	-	500	100	70
Single Pulse Energy (µJ)	-	4.68	30.89	50.14
Speed of Laser (mm/s)	-	100	132	150
Moving Energy Density (µJ/µm)	-	23.4	23.4	23.4
Hatch Spacing (µm)	-	300	300	300

2.3 Surface Characterisation

The depth mass concentrations profiles of the ASPN treated surface were measured and analysed using a glow-discharge optical emission spectrometer (GDOES; GDA 650 Spectruma Analytic Gmbh). Surface hardness was measured using a Mitutoyo MVK-H1 Vicker's microhardness tester with a load of 50 gram-force (gf). Raman spectroscopy was performed using a Renishaw inVia Raman Microscope fitted with a 488 nm excitation laser and a Raman

shift range of 250 to 2000 cm^{-1}. Finally, X-ray diffraction (XRD; Bruker D8 Advanced) using a Cu radiation source (Kα = 0.145 nm) was used to confirm the formation of the S phase.

Following surface texturing, scanning electron microscopy (SEM) imaging (JEOL 7000F) was used to examine the surface morphology, channel spacing and surface damage of each sample type. SEM imaging was also utilised on cross-sectioned and etched (50% HCl + 25% HNO$_3$ + 25% H$_2$O) samples in order to examine the texture layer morphology of each sample type. Energy-dispersive X-ray spectroscopy (EDS; Oxford Instruments Inca) was then used to perform in order to determine the chemical compositions of the textured surface S phase layers.

Cross-sections of the 310 fs textured samples were also prepared for transmission electron microscopy (TEM) using manual sample preparation (cutting and grinding) and a focussed ion beam milling (FIB; FEI Quanta 3D) approach to get the sample to nanometre thickness. Prior to milling, a protective platinum coating was deposited to shield the textured areas. A JEOL 2100 TEM was used to study the surface microstructure of the 310 fs textured S phase layer.

2.4 <u>1D Surface Temperature Modelling</u>

Surface temperatures (where depth = 0) during and following nanosecond pulses were calculated analytically using Fourier's second law [35]. Temperatures for the femtosecond pulses were not examined as they follow different mechanisms that are beyond the reach of this article [36]. Also, since the maximum temperature achieved with the laser was the main purpose of the calculation, material loss and phase changes (i.e. latent heats) were not taken into consideration for the heat flow. Additionally, since the maximum temperature is achieved at the laser spot, only one-dimensional heat flow was used for the calculation. The follow heating (equation 1) and cooling (equation 2) equations were used to calculate the temperature during and after each pulse [35].

$$T(t < \tau) = \frac{2I_0(1-R)}{k}.\sqrt{\alpha t}.\sqrt{\frac{1}{\pi}} + T_0 \qquad\qquad \text{(equation 1)}$$

$$T(t > \tau) = \frac{2I_0(1-R)}{k}.\sqrt{\frac{1}{\pi}}.\sqrt{\alpha}.\left[\sqrt{t} - \sqrt{t-\tau}\right] \qquad\qquad \text{(equation 2)}$$

where t is the time since the last pulse started (s), τ is the pulse duration (s), I_0 is the calculated laser intensity (equation 3); W.m^{-2}), R is the surface reflectivity at the wavelength of the laser source (value used is 0.6352), k is the thermal conductivity (16.3 W.m^{-1}.k^{-1}), α is the calculated thermal diffusivity (equation 4; m^2.s^{-1}) and T_0 is the starting temperature before the pulse begins (25 ° C) [37].

$$I_0 = \frac{E}{\tau\pi r^2} \qquad\qquad \text{(equation 3)}$$

$$\alpha = \frac{k}{C_p \rho} \qquad \text{(equation 4)}$$

where E is the energy of the pulse (J), r is the Gaussian spot radius (m), C_p is the specific heat of the material (500 J.Kg^{-1}.k^{-1}) and ρ is the material density (8000 Kg.m^{-3}).

The accumulation of heat with successive pulses was accounted for by re-calculating how long a pulse duration would have to be from the starting temperature to reach the temperature at the end of the last pulse (equation 5). The new pulse duration was then directly inserted into equation 2 in order to calculate each cooling cycle.

$$t(T) = \frac{\left[\dfrac{k(T - T_0)}{2I_0(1 - R)\sqrt{\dfrac{1}{\pi}}}\right]^2}{\alpha} \qquad \text{(equation 5)}$$

where T is the temperature reached just before the laser turns off (° C).

2.5 Electrochemical Corrosion Testing

2.5.1 Potentiodynamic Anodic Polarisation

Potentiodynamic anodic polarisation was performed to examine the response of the different sample types to corrosive conditions. Ringer's solution (9 g/L NaCl, 0.64 g/L CaCl.2H$_2$0, 0.42 g/L KCl and 0.2 g/L NaHCO$_3$), which closely resembles body fluid, was used as the electrolyte solution for all of the tests [38]. A Gammry Interface 1000 instrument was used to measure current changes during the experiments. An open circuit potential test was initially performed for 3600 seconds to stabilise the surface voltage and obtain an estimated corrosion potential (E$_{OC}$). Anodic polarisation was then performed between -0.5 mV and 1.5 mV of the obtained E$_{OC}$ at a scan rate of 2 mV/s. Following the tests, SEM imaging of the surfaces were used to look at the morphology of the samples as well as measure the total length of laser created channels within the tested areas for each sample. Additionally, cross-section SEM imaging was also used to roughly measure the extra surface area provided by the channels. By multiplying this extra surface by the total length of the channels in the test area it was possible to approximate the surface area tested for each electrochemical test performed. Tafel curve fitting was then utilised to determine the corrosion potential (E$_{Corr}$), corrosion current density (I$_{Corr}$) and corrosion rates of each sample type.

2.5.2 Electrochemical Impedance Spectroscopy

Electrochemical impedance spectroscopy (EIS) analysis was carried out using a Gammry Interface 1000 instrument. EIS testing was carried out following an open circuit potential test

performed for approximately 5400 seconds. The EIS test was performed using Ringer's solution, an AC amplitude of ±10 mV and a frequency range between 10^{-2} and 10^5 Hz with 10 points per decade.

3   Results

3.1   ASPN Surface Layer

The as-treated sample type was used to determine the conditions of the surface layer prior to texturing. Elemental depth profiling revealed an approximately 8 µm deep nitrided surface layer. Semi-quantitative measurements from GDOES also demonstrated a maximum nitrogen content at the surface of approximately 20 at% (Figure 1A), with an improvement in hardness from 200 to 1130 (HV0.05) following treatment, which are all typical for an S phase surface treatment [10]. Cross-section SEM micrographs (Figure 1B) confirmed the presence of a precipitate free S phase surface layer measuring approximately 8.17 ± 0.4 µm deep, which agrees with the depth profiling data (Figure 1A). X-ray diffraction data (Figure 2) further confirmed the formation of the S phase on the as-treated samples with characteristic left shifted austenite (ϒ) peaks at 42 ° (S1) and 47 ° (S2) without any appreciable peaks for chromium nitrides. Additionally, the ϒ(111) peak, present from the underlying bulk material, can also be seen at a 2θ angle of 44 °.
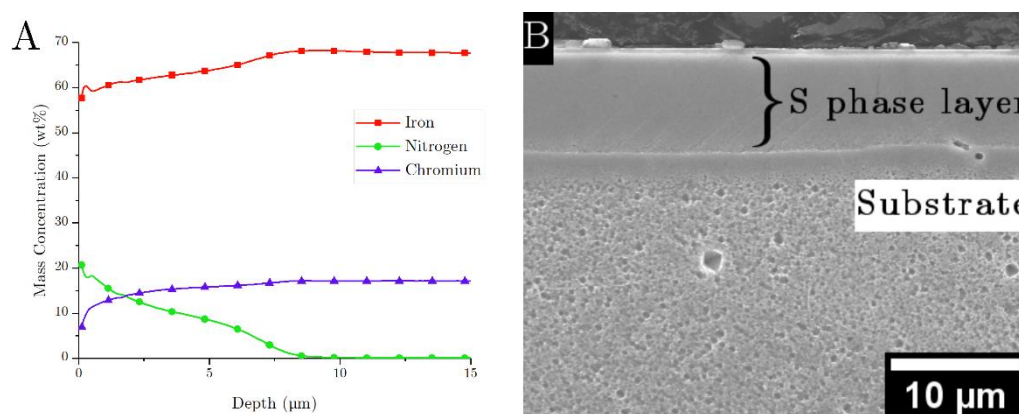

Figure 1 Characterisation of the as-treated sample type. (A) shows elemental depth profiling and (B) shows the cross-sectional morphology of the S phase.
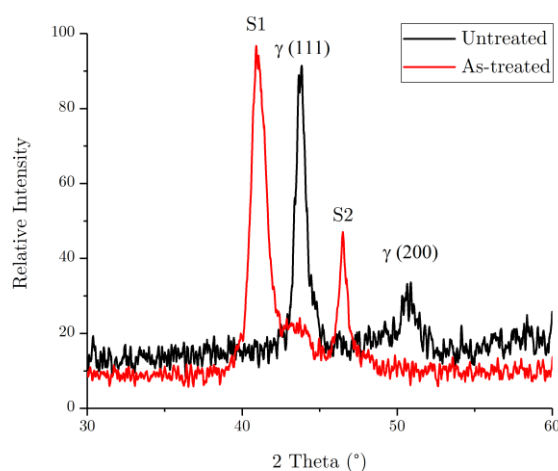

Figure 2 XRD phase comparison of untreated and as-treated treated samples.

3.2 <u>Morphology of Textured Surfaces</u>

From the electron micrographs (Figure 3) it is clear to see that the spacing of the channels are consistent with the set hatch spacing of 300 μm. However, it is also obvious that the width of the channels varies between sample types. The channel widths become larger with increasing pulse duration, going from 29.97 ± 1.4 μm for the 310 fs sample type, to 52.44 ± 3.3 μm for the 220 ns sample type. The morphology of the tracks and the surrounding areas also varies greatly. Clear signs of melting and recasting are visible in both of the 15 ns and the 220 ns samples, with re-solidified metal droplets being spread within and around each channel (Figure 3B3 & C3) [14]. The 15 ns textured samples display a smooth and perpendicularly layered inner track with regular surface cracking. The 220 ns textured samples demonstrate the most drastic change in surface morphology, with the presence of vast amounts of droplets, especially within each channel. Additionally, the 220 ns tracks appear to have segments whereby the channels close in on themselves. On the other hand, the 310 fs textured samples present with minimal change in surface morphology to the surrounding areas of the channels. Fine nanoscale debris and particulates are present adjacent to channels, which most likely arise due to the ablation and back sputtering that occurs during the texturing process (Figure 4B) [39]. No obvious signs of melting or cracking can be deduced from the surface images. Also, typical sub-micron ripple-like LIPSS textures can be clearly seen within the channels (Figure 4A). Altered periodicity, changing orientation and presence of holes can be seen within the channels, which are likely to be as a result of incomplete optimisation of the laser source and should be considered for the morphology of the surface following electrochemical corrosion testing.
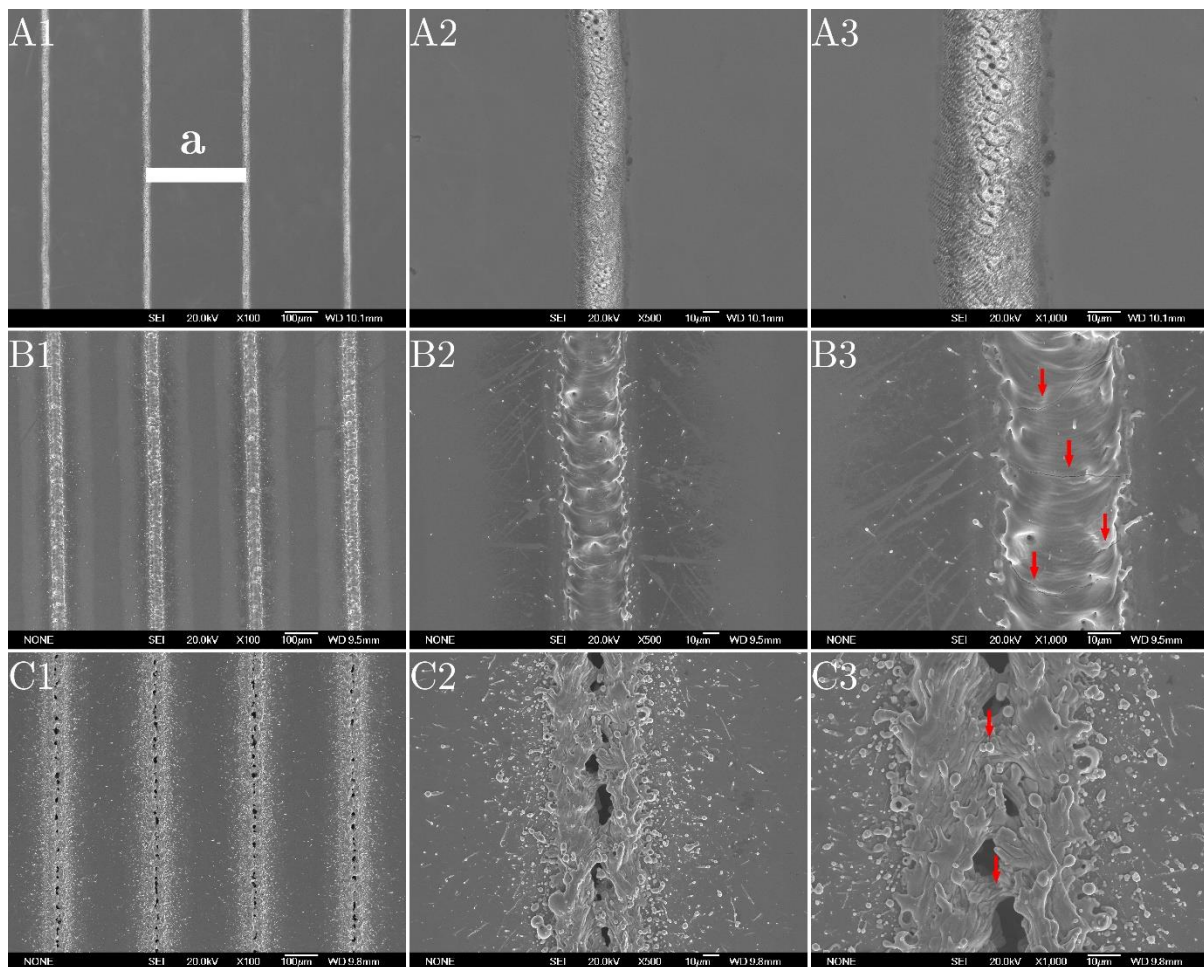
Figure 3 Surface morphology of the textured samples. (A1-3) 310 fs samples, (B1-3) 15 ns samples and (C1-3) 220 ns samples. Hatch spacing (a) was also measured to be 300.6 ± 1.1 µm. Arrows indicate areas where cracks are present and where channels have closed in on themselves.

Figure 4 Surface morphology of 310 fs textured samples. The fine sub-micron ripple textures along each channel can be seen in image A, with some inconsistencies in the texturing process (a). Image B shows the back-sputtered particulates (b) found adjacent to the channels.

3.3 <u>Cross-sectional Layer Structure</u>
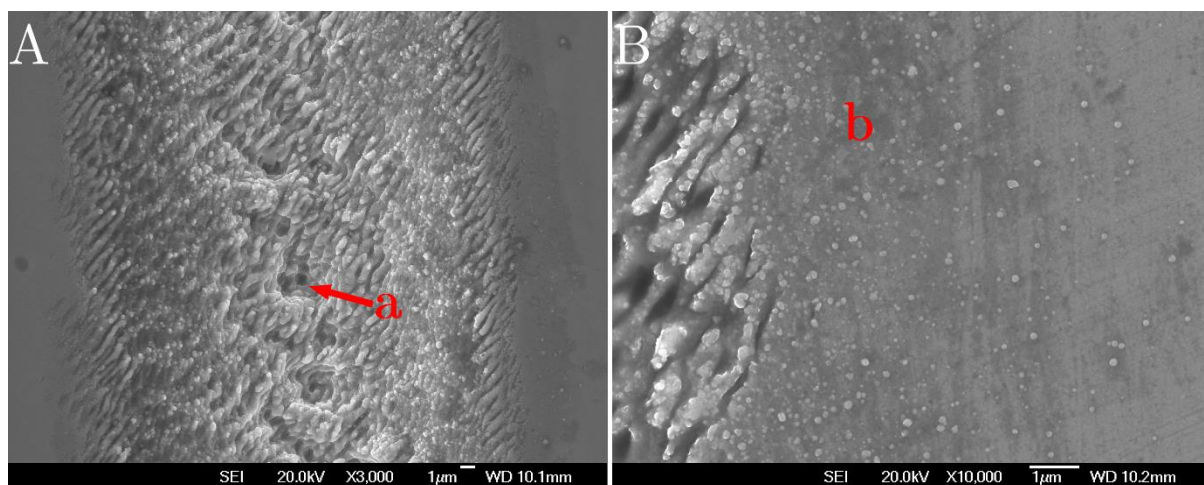
Comparisons of the structures underneath and around the laser textured channels were made with the as-treated sample type (Figure 1B) to determine any changes or damage to the S phase. Other than the addition of the channels and LIPSS textures, no visible changes can be distinguished in the cross-sections of the 310 fs treated samples (Figure 5A1-3). Even under backscattered electron imaging, no variation in contrast density can be seen (Figure 5A3). EDS mapping (Figure 6A & B) also helped to show no discernible changes to the elemental profile across the 310 fs channels. On the other hand, both nanosecond laser textured samples displayed clear signs of damage to the surface layer. Obvious cracks can be seen near the surface of the 15 ns textured samples (Figure 5B2-3), while complete loss of the S phase is observed within and atop of the channels in the 220 ns textured samples (Figure 5C1 & 6D). Moreover, EDS mapping of the cross-sectional areas of the nanosecond textured samples conclusively show the altered elemental profile (Figure 6B & C). In particular, the formation of localised areas of high chromium, high nitrogen, low iron and low nickel in the superficial regions of the textures (as indicated in Figure 6) help to confirm the presence of chromium nitrides. Additionally, both nanosecond textured samples also present clear signs of general compositional changes at the surface (Figure 5B3 & C3) and initiations of the formation of lamellar structures (Figure 5B2-3 & C2-3). Confirmation of the composition of these formations was made using EDS spot analysis (Table 2).

Table 2 shows the changing chemistry within these regions in comparison to surface composition data from as-treated samples. A clear increase of Cr, N and Mo was detected on the 15 and 220 ns textures samples, with the latter showing the greatest increase. However, the concentration of Fe and Ni were reduced following both ns textures (also found under EDS mapping (Figure 6)). Again, the most profound changes were observed following the 220 ns texturing. On the other hand, the only observable changes found with the 310 fs textured samples were with the detected compositions of S and Mn, which were both only slightly altered.
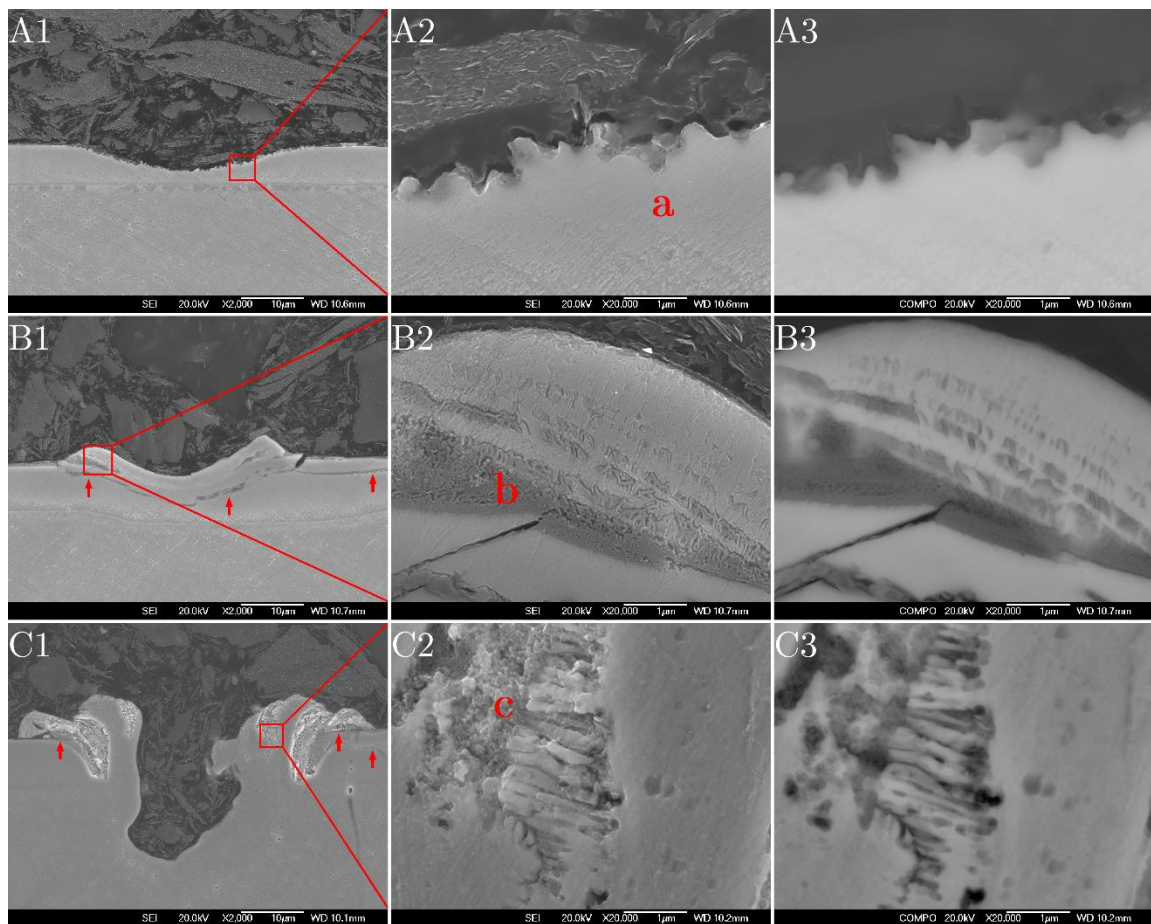
Figure 5 Secondary (A1-A2, B1-B2 and C1-C2) and backscattered (A3, B3 and C3) electron images of cross-sectional layer structures of the textured samples. (A1-A3) 310 fs samples, (B1-B3) 15 ns samples and (C1-C3) 220 ns samples. Areas of material cracking are indicated with an arrow. Labels (a, b and c) indicate locations of elemental spot analysis listed in Table 2.
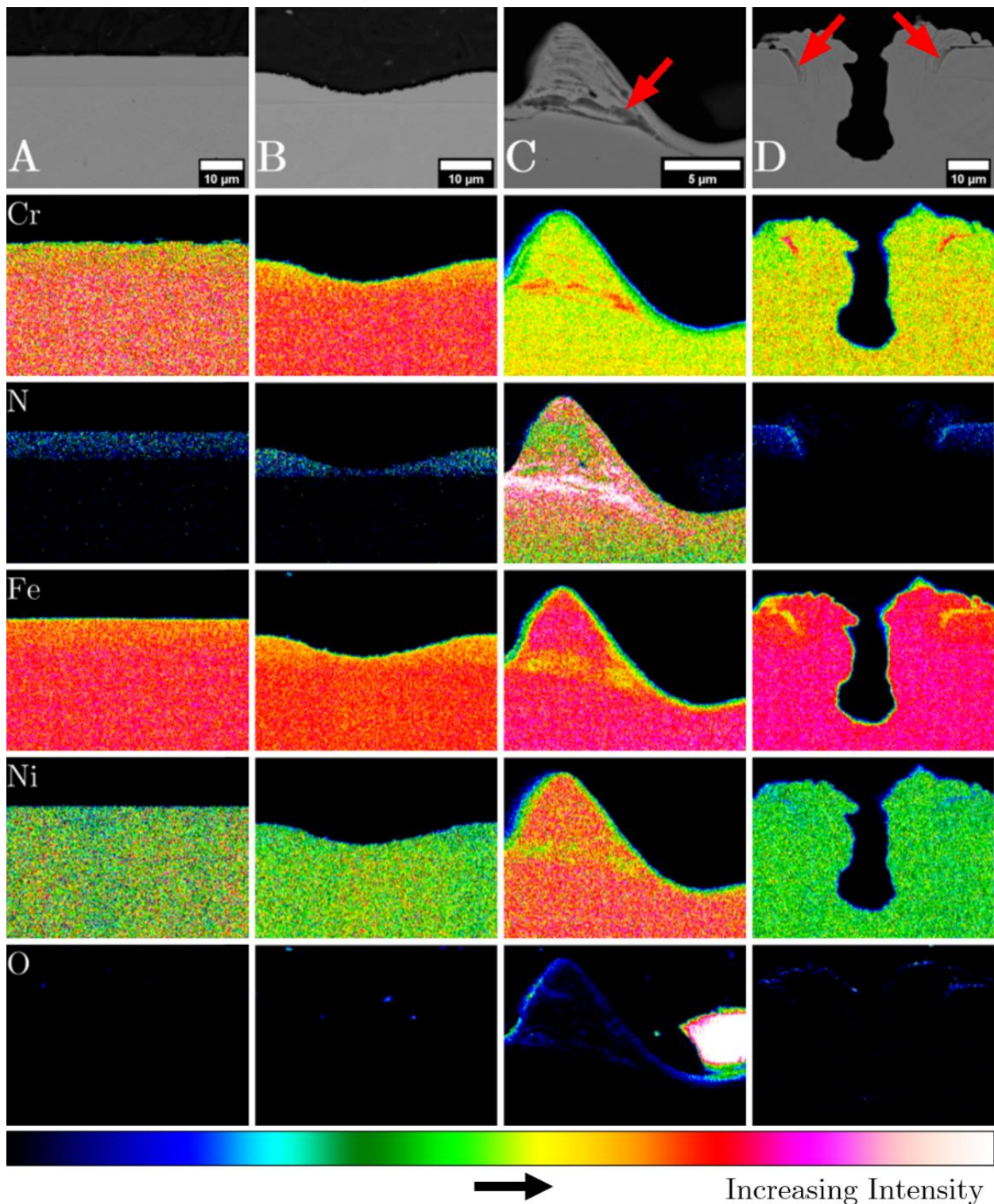
Figure 6 Backscattered electron imaging (top row) and EDS elemental mapping through the cross-sectional areas of each sample type: (A) as-treated samples, (B) 310 fs textured samples, (C) 15 ns textured samples and (D) 220 ns textured samples. Samples are organised in columns, with each row representing a different element (as labelled). Colour intensity mapping used is relative to each individual element map. Arrows correspond to sites of precipitation that match elemental composition changes in the related maps.

Sample	Cr	Fe	N	Ni	Mo	Mn	Si	S
As-treated	16.73	65.08	4.32	9.73	1.75	1.88	0.48	0.03
310 fs	16.40	66.34	4.10	9.52	1.66	1.58	0.36	0.04
15 ns	21.10	61.45	5.77	7.49	2.01	1.88	0.25	0.05
220 ns	24.86	51.17	10.08	8.95	2.99	1.54	0.41	0.00

The formation of the lamellar structures (Figure 5) and compositional changes (Table 2 & Figure 6) on the nanosecond textured samples have already demonstrated the formation of chromium nitrides precipitates, and hence TEM analysis was not carried out on these sample types [40]. Instead, TEM analysis was carried out to conclusively confirm whether the S phase on the 310 fs samples had remained precipitate free. As the textured surface was directly in contact with the femtosecond laser beam, a protective layer of Pt was deposited before ion beam cutting and milling (Figure 7A). Cross-sectional TEM microstructures shown in Figure 7B and C revealed the contours of the texture at the top surface. Observations at the areas just beneath the contour line confirmed no CrN precipitation (Figure 7B & C). Selected area diffractions taken from the S phase area showed FCC structured patterns (Figure 7D) with expanded austenite d-spacing, consistent with expected XRD data [10]. High density microstructure defects, such as micro-twins (Figure 7B) and dislocations, were presented within the layer, which are the characteristic of the S phase layer [10, 26].
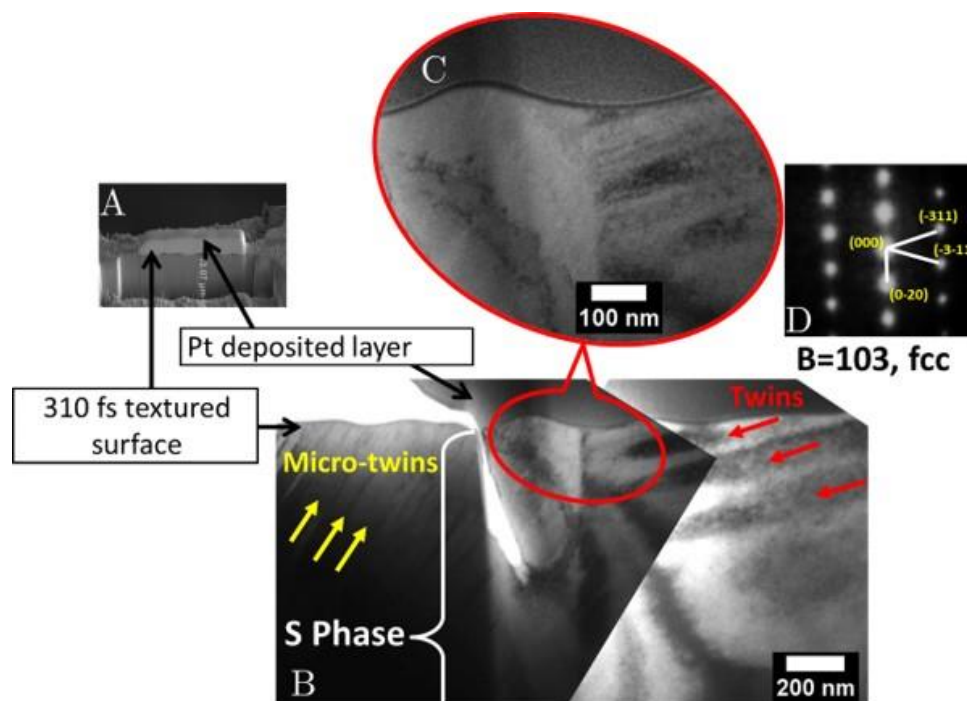

Figure 7 Cross-sectional TEM sample preparation and characterisation of the 310 fs textured sample: (a) SEM image of FIB cutting and milling sample for a thin TEM specimen; (b) TEM image of the S phase layer, showing surface texture contour line; (c) enlarged 310 fs textured top surface, and (d) selected area diffraction pattern from S phase area shown in (c).

3.4 <u>Predicted Surface Temperature</u>

To attribute the rapid deterioration of the S phase following nanosecond texturing, 1D heat conduction modelling was carried out to predict the maximum possible temperatures at the surfaces of the samples following single (Figure 8) and multiple (Figure 9) pulses from the laser source. No sources of heat loss (e.g. phase changes & material loss) other than conduction has been accounted for in the model. Therefore, in both cases (single and multiple pulses) it can be thought of as the maximum possible temperature following laser heating. The peak temperatures (T_{peak}) vary greatly between the two laser settings; the 15 ns pulses achieving approximately 18000 °C after a single laser pulse, while the 220 ns pulse reaching a much lower, but still incredibly high, temperature of around 8000 °C (Figure 8). Following multiple pulses, only a limited amount of heat accumulation occurs before an equilibrium between the heating and cooling rates is achieved (Figure 9). Although counterintuitive, the higher temperatures reached following a shorter pulse can be explained as a result of the much greater laser intensity of the 15 ns pulse (2.91x10^{12} Wm^{-2}) in comparison to the 220 ns pulse (3.22x10^{11} Wm^{-2}).

The cooling rates of both pulse durations follow a similar trend, leading to a saturation temperature (T_{sat}) of 390 °C for the 15 ns pulses and 577 °C for the 220 ns pulses. Additionally, by taking an average temperature across the data in Figure 9 and then calculating the time taken for the laser to move the distance of one spot diameter (Table 1) it is possible to approximate the temperature (757.24 °C (15ns) and 1111.45 °C (220 ns)) and length of time (227.27 μs (15 ns) and 200 μs (220 ns)) any one spot on the sample will be subjected to. Similarly, using extended version of the data presented in Figure 8, it is also possible to predict average temperatures for single pulses of each laser (729.2 °C (15 ns) and 981.8 °C (220 ns)).
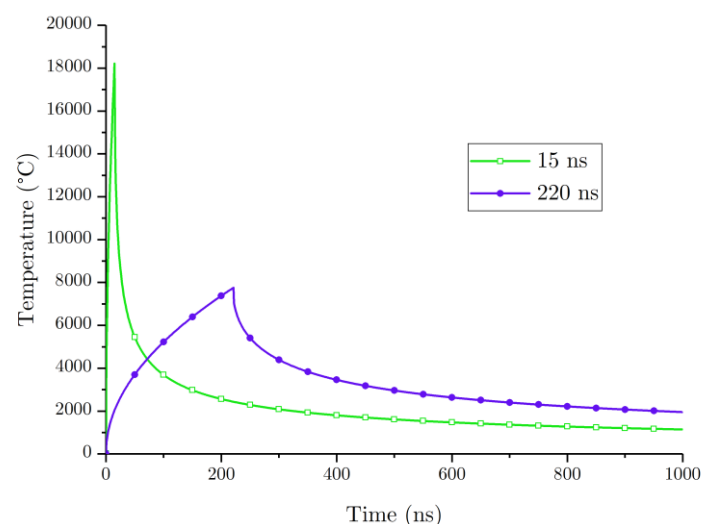

Figure 8 Single pulse surface temperature modelling following 15 ns and 220 ns laser pulses.
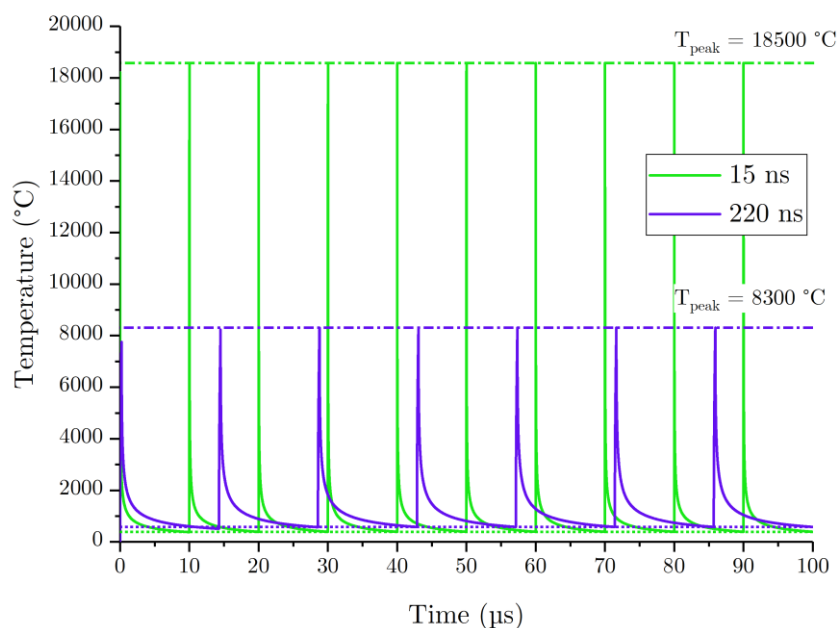
Figure 9 Multiple pulse surface temperature modelling following 15 ns and 220 ns laser pulses. Dash and dot lines indicate the peak temperatures, while the dotted lines show the saturation temperatures.

3.5 <u>Corrosion Behaviour</u>

3.5.1 <u>Potentiodynamic Anodic Polarisation</u>

The calculated corrosion rates (Table 3) demonstrated that the as-treated and 310 fs textured samples possessed the best average resistance to corrosion (4.5 and 30.2 μm/year, respectively) across the tested area. Both sample types displayed drastically better predicted corrosion rates than the 15 ns (264.4 μm/year) and 220 ns (685 μm/year) textured samples. Correspondingly, the corrosion current density (I_{Corr}) follows the same trend for all sample types. Corrosion potential (E_{Corr}) data revealed that the polished and femtosecond textured samples (-206 and -218 mV/SCE, respectively) were the most noble. On the other hand, the 15 ns textured samples showed the most negatively charged corrosion potential (-567 mV/SCE). The 220 ns textured surface displayed a more noble corrosion potential (-294 mV/SCE), which can be attributed to the vast oxidation that occurs during thermal laser texturing [14].

Table 3 Quantitative corrosion measurements of each sample type.

	As-treated	310 fs	15 ns	220 ns
I_{corr} (μA/cm²)	0.392	2.61	22.8	59.1
E_{corr} (mV/SCE)	-206	-218	-567	-294
Corrosion Rate (μm/year)	4.5	30.2	264.4	685.0

The polarisation curves (Figure 10) match up clearly to the calculated corrosion potentials. As expected, multiple signs of re-passivation are obvious on the as-treated samples. The 15 ns textured samples also show signs of current density stagnation between the potentials of approximately -0.3 and 0.2 mV/SCE. Almost no signs of passivation can be observed with the 220 ns textured samples, while, only limited passivation is present on the femtosecond textured samples.
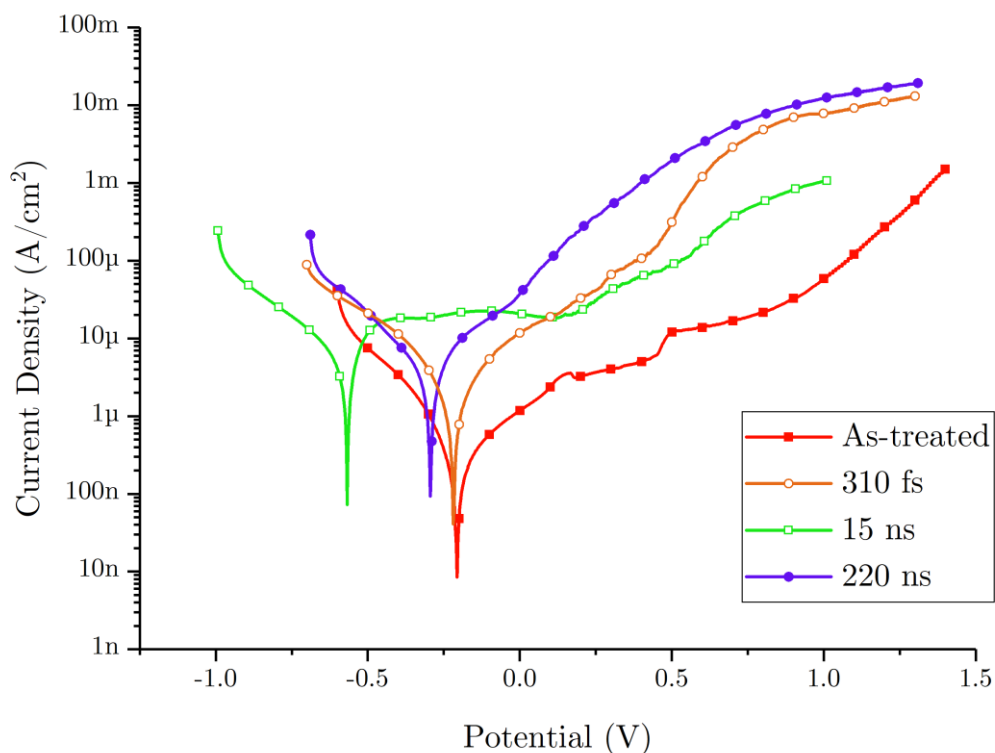

Figure 10 Polarisation curves of the different sample types in Ringer's solution.

Surface SEM imaging was carried out following anodic polarisation testing in order to observe the condition of the textured surfaces (Figure 11). Vast damage to the surface structure can be seen on both nanosecond textured samples. On the surface of the 15 ns samples, grain boundary corrosion related to the precipitation of chromium nitrides can be clearly distinguished (Figure 11B1-2) [10]. Whereas, the surface of the 220 ns samples reveal large amounts of cracks perpendicular to the channels as a result of the thermal shock following the rapid heating and cooling cycles [14]. On both nanosecond textured samples there are sign of partial (15 ns) and complete (220 ns) removal of the bulges at the sides of the channels (Figure 11B & C). On the other hand, the 310 fs channels show almost no change or damage to the surface, even under backscattered electron imaging (Figure 11A1-2). In particular, the fine LIPSS textures within the channels demonstrate excellent resistance to the Ringer's solution, despite the vastly greater surface area.
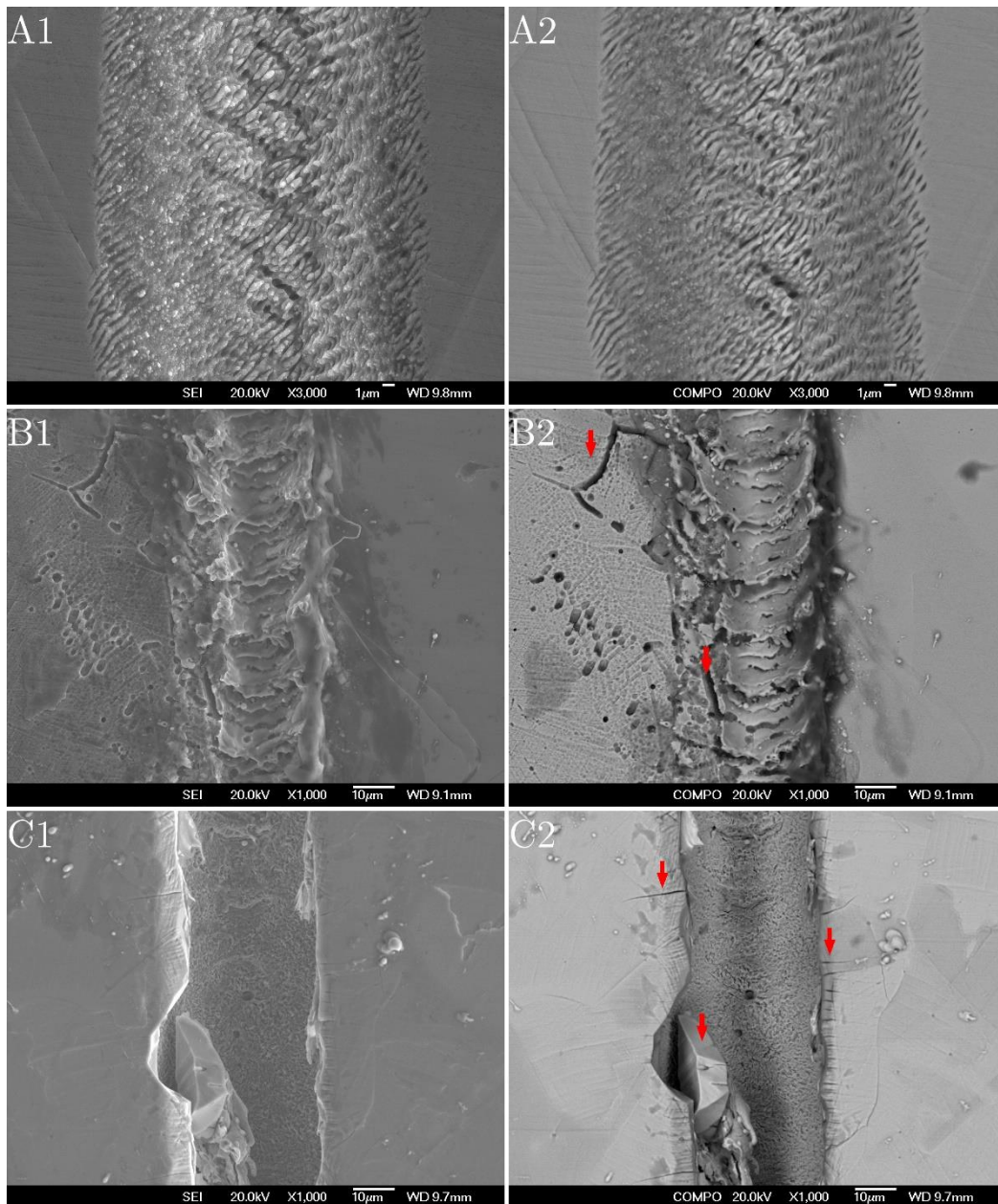
Figure 11 Secondary and backscattered electron imaging of textured surfaces following anodic polarisation testing. Arrows indicate areas of material damage or profound corrosion attacks.

3.5.2 **Electrochemical Impedance Spectroscopy**

The Nyquist (Figure 13) and Bode plots (Figure 12) both demonstrate correlating results to the data obtained through anodic polarisation testing, with the best total resistance to polarisation (R_f + R_p) being found in the as-treated and 310 fs textured samples (Table 4). The superior impedance (real component, imaginary component and total magnitude) of these surfaces over the nanosecond textured surfaces can be further discerned from the data obtained at the lowest frequency (10^{-2} Hz). Additionally, the phase angle differences in the bode plots (Figure 12) indicate a change in surface structure with the nanosecond textured surfaces, whereas almost identical trends are captured with the as-treated and 310 fs textured samples. This is particularly highlighted by the different equivalent circuits used for each sample type fitting (Figure 14), with both nanosecond textured surfaces demonstrating some form of diffusion based impedance (Warburg impedance) that can be attributed to the formation of a thick porous surface oxide layer as a result of the rapid heating and cooling laser texturing process (Figure 6) [14, 41]. Furthermore, data collected from Raman spectroscopy (Figure 15) also help to confirm the presence of the oxide (as well as some carbon deposits) following laser texturing [42, 43].

Table 4 Measurements of resistance to polarisation of each sample type.

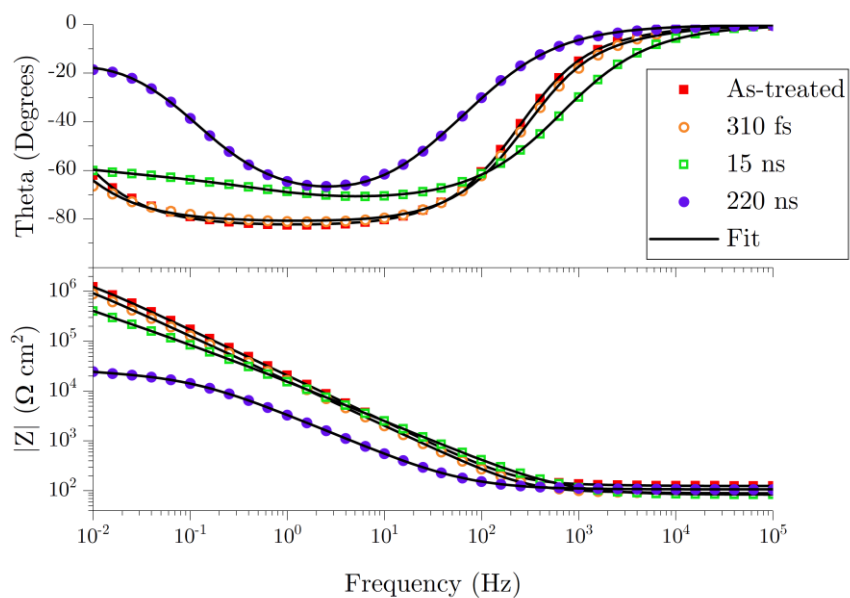|	As-treated	310 fs	15 ns	220 ns
R^f	58.98	43.80	1.93×10^5	2096
R_p	3.202×10^6	3.203×10^6	404.8	1.97×10^4
R_{Total}	3.202×10^6	3.203×10^6	1.93×10^5	2.18×10^4

Figure 12 Bode phase (top) and magnitude (bottom) plots of all sample types. Fitted lines were made according to the equivalent circuit models in Figure 14.
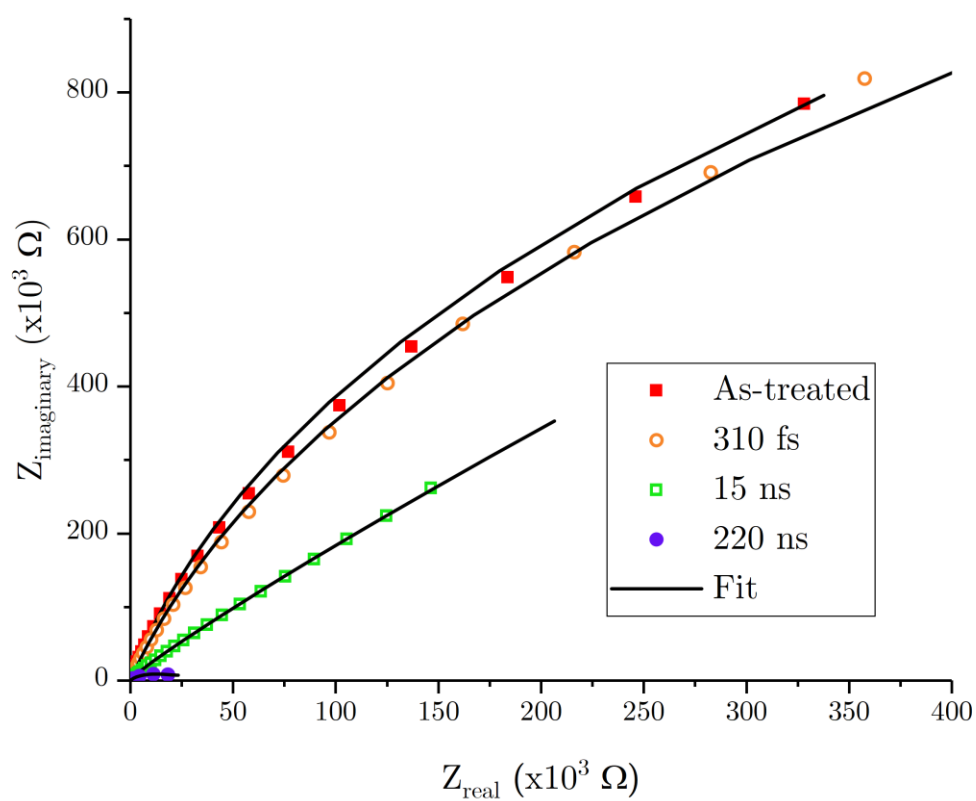
Figure 13 Nyquist plot of Impedance of all sample types. Fitted lines were made according to the equivalent circuit models in Figure 14.
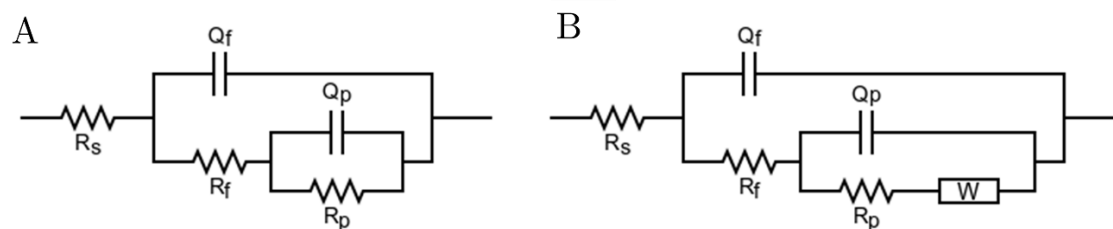
Figure 14 Equivalent circuits models used for EIS analysis where R_s is solution resistance, R_f (resistance to polarisation) & Q_f (double layer capacitance) relate to the outer liquid interface layer, R_p & Q_p relate to the S phase/untreated bulk barrier, and W relates to the Warburg impedance associated with diffusion resistance . Model A was used for as-treated and 310 fs textured samples. Model B was used for 15 ns and 220 ns textured samples.

Figure 15 Raman spectroscopy of all sample types. Peaks relating to surface carbon deposition and surface oxidation are labelled accordingly.

4   Discussion

The precipitation of chromium nitrides following low-temperature plasma nitriding of stainless steels is usually used as an indicator for a poor or failed treatment. Much of the literature states that this formation has detrimental effects on the corrosion resistance of the surface [44]. Although chromium nitrides themselves possess excellent corrosion resistance, 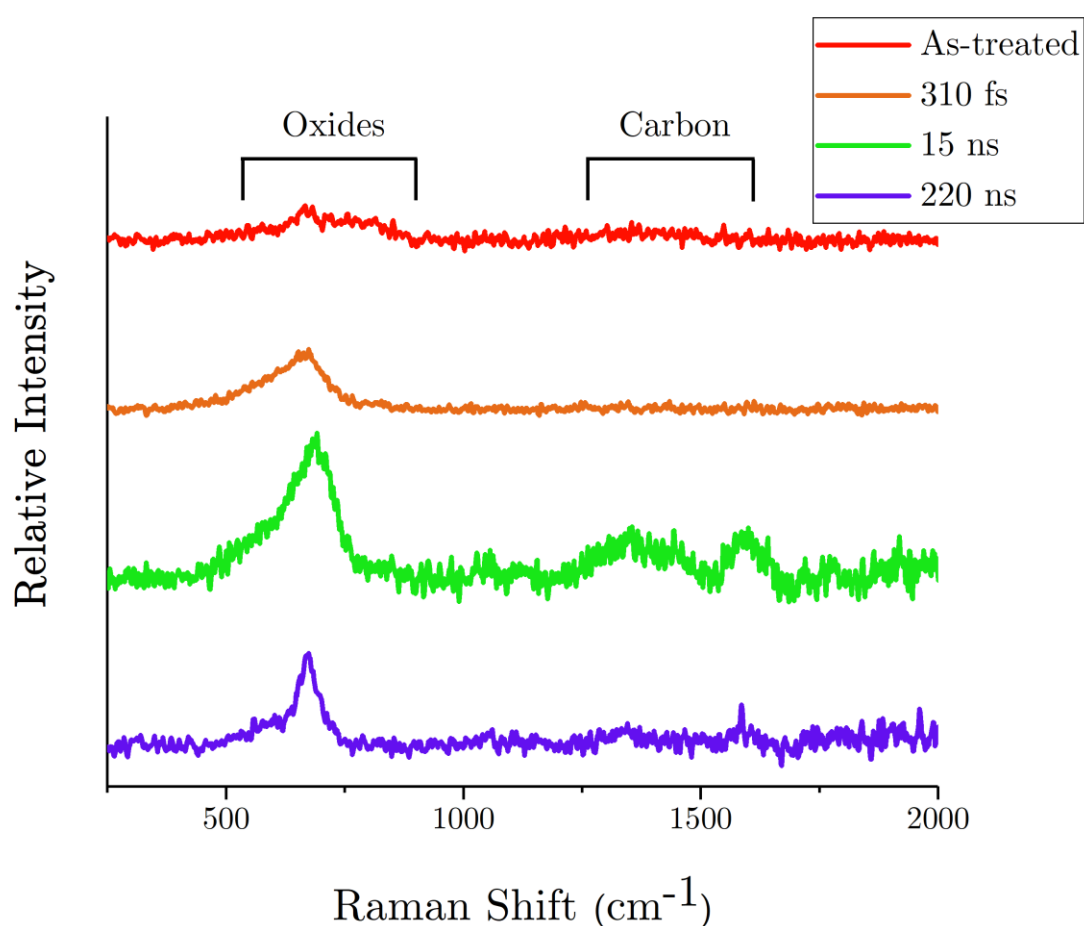however, the issue with the formation of these precipitates is the effect that they have on the surrounding material. In stainless steel, the corrosion resistance is obtained through the formation of the continuous passive chromium oxide (Cr_2O_3) film [45, 46]. When the distribution chromium becomes inhomogeneous and in some local areas its content is below the minimum value required for stainlessness, like it does within adjacent areas to chromium nitrides, it leads to the breakdown of the protective layer, which subsequently causes the deterioration of the corrosion resistance [21, 27, 47]. This has been supported by the electrochemical test results shown in Figure 10-14 & Table 3-4. Therefore, it is important to avoid precipitation of chromium nitrides and the decomposition of S phase during laser surface texturing

Laser energy transfer onto material surfaces is known to predominantly occur through absorption by valence electrons [36, 48]. Significant transfer of energy between the electrons and the surrounding lattice has also been shown to take approximately 1 picosecond (10^{-12} s). Therefore, pulsed laser texturing, even down to nanosecond (10^{-9} s) pulse durations, always involves the heating of surface matter to create textures. This obviously requires high temperatures that increase the risk of decomposition of the S phase.

4.1   Response of S Phase to Nanosecond Texturing

Kinetic analysis is a common approach that can be utilised to analyse the response of a material to heating. Additionally, it has already been implemented successfully to predict the degree of precipitation that can be expected following heating and annealing of an S phase through-treated material. Due to the success of this approach it is only natural to also apply the same technique to predict if decomposition of the S phase will occur following nanosecond laser texturing. Owing to the rapid heating and cooling of the patterned areas (Figure 8 & 9), laser texturing can be regarded as a non-isothermal heat treatment of the surface. Therefore, following on from the work by Christiansen et al. [49], calculations were carried out to determine the expected degrees of precipitation following laser texturing using equations for non-isothermal isochronal annealing (equation 6 & 7).

The results suggest that, in both 15 ns and 220 ns textured surfaces, there should be complete decomposition (f = 1) of the S Phase. Seemingly, this does not directly match the observed outcomes following the texturing (Figure 5). However, upon more careful analysis of the results, the calculated transformed fractions are likely to be true. Firstly, as predicted through the simulations (Figure 8 & 9), the immediate surface temperatures (18000 and 8000°C for 15 and 220 ns pulses respectively) expected during the texturing are comfortably more than the melting point of the 316L stainless steel. This implies that the superficial S phase material is melted and can easily be pushed away or removed during the texturing. This is evidenced by the pile-up of material along both sides of the laser channels as shown in Figure 3B1 and

the key-hole shown in Figure 3C1. By combining both arguments it is easy reach the conclusion that the missing material, that physically leaves the voids that create the textures, would have been decomposed. Therefore, if we consider a scenario whereby the melted/ablated matter remained in position, it would be expected that this S phase material would be fully decomposed, and hence, in accordance with the calculated fractions transformed.

$$f = 1 - \exp[-\beta^n] \qquad \text{(equation 6)}$$

$$\beta^n \ (non-isothermal) \approx \left[\frac{k_0 . \varphi . R . \left[t + \frac{T_0}{\varphi} \right]^2}{Q} . exp \left[\frac{-Q}{R . \varphi . \left[t + \frac{T_0}{\varphi} \right]} \right] \right]^n \qquad \text{(equation 7)}$$

where f is the fraction transformed, β is the path variable, n is the Johnson-Mehl-Avrami equation for heterogeneous reactions, k_0 is the pre-exponential factor (s^{-1}), φ is the heating rate (k.s^{-1}; 48816000000 k.s^{-1} for 15 ns and 4938409091 k.s^{-1} for 220 ns), R is the gas constant (8.31446 J.mol^{-1}.k^{-1}), t is the time held at this temperature (s; 227.27 µs for 15 ns and 200 µs for 220 ns), T_0 is the starting temperature (298 k) and Q is the overall activation energy (139000 J.mol^{-1}).

The observed decomposition of the S phase material adjacent to the laser channel or beneath the 15 ns and 220 ns textured surfaces can be explained using the predicted average temperature (Section 3.4). Since nanosecond laser texturing is known to be a thermal process it is possible to apply Fourier's second law (heat conduction) in order to predict whether enough mobility is introduced into the surface to initiate the formation of precipitates [36]. Chromium nitrides that form within nitrided surfaces of stainless steels predominantly have the empirical formula of CrN that grows with a face-centred cubic (fcc) crystal structure [40, 50]. It is already known that interstitial elements such as nitrogen can move significantly more freely through the lattice than substitutional elements such as chromium. Therefore, it can be deduced that the determining step for the initial formation of chromium nitrides is directly related to the mobility of chromium atoms. The minimum amount of diffusion necessary to initiate the precipitation of a chromium nitride would require the movement of one chromium atom at least the distance of one lattice parameter of CrN (0.414 nm) [25, 40]. In this case, it is assumed that all the other randomly distributed elements, by chance, already occupy the necessary positions to initiate the formation of CrN [10, 51].

Combining this logic with the data from the models allows for the prediction of whether, in theory, it is feasible to form chromium nitrides following nanosecond texturing. By using diffusion coefficient calculations (D; equation 8 & 9) for Cr in austenite with the average temperatures and durations predicted in the results section, it is possible to estimate the expected distance that Cr atoms are able to move during the time that the surface is heated (equation 10). The diffusion equations are based on experimental data obtained from radiotracer (equation 8) and microprobe analysis (equation 9) [52]. Table 5 shows that in

both nanosecond laser texturing settings it is more than feasible for chromium nitrides to precipitate. In fact, even when repeating the same process for a single pulse of each laser setting it was still found to provide much greater than the minimum movement (355-546 nm (220 ns) and 41-61 nm (15 ns)) required for the chromium atoms to form nitrides (0.414 nm) (Table 5).

$$D = [10.8].exp\left[\frac{-69700}{R.T}\right] \qquad \text{(equation 8)}$$

$$D = [4.08].exp\left[\frac{-68500}{R.T}\right] \qquad \text{(equation 9)}$$

$$x = \sqrt{D.t} \qquad \text{(equation 10)}$$

where D is the diffusion coefficient (m^2.s^{-1}), R is the gas constant (8.31446 J.mol^{-1}.k^{-1}), T is the temperature (k), x is the distance travelled (m) and t is the time (s).

Table 5 Total distance of chromium diffusion for any surface spot following nanosecond laser texturing.

	Average Temperature (°C)	Diffusion Coefficient of Cr in γ-Fe (x10^{-7} m^{2}s^{-1})	Time (µs)	Distance Travelled (nm)	Equation
220 ns	1111.45	25.30209408	227.27	23980	equation 8
		10.60906831		15528	equation 9
15 ns	757.24	3.15713621	200.00	7946	equation 8
		1.37206785		5238	equation 9

In agreement with both kinetic analysis and the Cr diffusion predictions, both nanosecond texturing processes were found to cause decomposition of the S phase. This is most clearly demonstrated with the presence of chemically altered regions under cross-section SEM imaging (Figure 5B3 & C3) and EDS mapping (Figure 6C & D). In both cases, the precipitated areas formed at the lips of the channels present with rod and lamellar structures that arise from the formation of nitrides interlaced with austenite [40]. Additionally, the increasing concentrations of Cr, N and Mo (Table 2 & Figure 6) within these darkened areas following chemical etching of the material further confirmed the presence of precipitates (Figure 5).

Electrochemical corrosion results (Figure 10 & Table 3) emphasised the decomposition of the S phase and the presence of the precipitates by demonstrating drastic increases in the corrosion rates of both of the nanosecond textured samples [53]. Additionally, this is highlighted by the drastic reduction in impedance (Figure 12 & 13) & total resistance to polarisation (Table 4) following nanosecond texturing, which occur due to the decomposition of the surface S phase layer. This is also supported by the change in phase angles across the EIS study; which demonstrate a change in surface structure of the nanosecond textured

samples in comparison to the as-treated sample type. The effect of the nanosecond laser heating is further exhibited through the rapid formation of a thick porous surface oxide layer (300-500 nm for 15 ns, and 600-700 nm for 220 ns; Figure 6). This is also supported by the presence of oxide peaks in Raman spectroscopy (Figure 15). The presence of intergranular damage and quench cracking (Figure 11) on the samples also outline the thermal shock effect of the laser on the surface.

4.2   Response of S Phase to Femtosecond Texturing

Based on the data obtained, it can be deduced that the femtosecond laser texturing is suitable for use in combination with the S phase. No discernible change in composition (Table 2 & Figure 6), morphology (Figure 5) or CrN precipitates (Figure 7) could be detected following the texturing. In particular, the lack of other crystal structures, such as hexagonal closed packing (hcp; Cr_2N), or nanocrystalline phases, under TEM electron diffraction conclusively confirmed the precipitate-free nature of the S phase [40]. Additionally, the femtosecond texturing also did not lead to the development of detrimental defects such as cracking observed with the nanosecond laser channels (Figure 3) or the pile-up of materials along the both side of laser channels (Figure 5). In the future, further studies using X-ray photoelectron spectroscopy (XPS) could also help to confirm the damage-free and chemically unaltered structure of the metastable S Phase following femtosecond laser texturing.

This is ultimately because during femtosecond laser texturing enough energy is provided within the extremely short pulse duration to cause evaporation of the irradiated surface. The consequence of this is that fine evaporation (ablation) occurs at the laser spot without, in theory, any opportunity for heat to be transferred to the surrounding material [34, 36, 54]. This idea is supported by the lack of any observable oxide layer (Figure 6), that would be expected to form had the surface been exposed to heat, on the femtosecond textured samples. Hence, femtosecond laser texturing provides a promising route for the patterning of S phase treated surfaces to produce wear resistant, corrosion resistant and functionalised stainless steel surfaces capable of being used in the food and medical industries.

As previously discussed (Section 1), the lack of research into laser texturing of S phase surfaces has been due to the damaging effect it is thought to have on the corrosion resistance of the surface. Therefore, to confirm the viability of femtosecond laser texturing for use with S phase surfaces, it is necessary to demonstrate the retained corrosion properties. As evidenced in Figure 10, no appreciable change in corrosion potential was observed following 310 fs texturing. Although the corrosion rate and current density did increase slightly, this is likely due to the difficulties associated with the accurate quantification of sub-micron textured surface areas (Figure 4) [55]. If the increased surface area could be accounted for, then both the current density and corrosion rate would be expected to match the values for the as-treated surfaces. Indeed, the lack of any observable damage (Figure 11) following the anodic polarisation testing also suggests the retention of the precipitate-free homogeneous S phase [10]. Furthermore, the similarities between the total resistance to polarisation, impedance (real, imaginary and total magnitude) and phase angle all suggest that no

significant change occurred to the surface chemical structure following femtosecond texturing.

5   Summary and Conclusions

In this study, the effect of ultrashort (nano and femtosecond) laser texturing on the microstructure and properties of S phase treated surfaces has been investigated, both theoretically and experimentally, for the first time. The following conclusions can be drawn from the research:

- Surface texturing using laser pulses within the nanosecond (ns) regime (15 and 220 ns) led to the severe damage of the S phase surface, decomposition of the metastable S phase and formation of precipitates. Subsequently, distinct losses in corrosion resistance were revealed through anodic polarisation testing & electrochemical impedance spectroscopy;
- Heat conduction modelling revealed that nanosecond pulsed laser texturing provided significantly higher temperatures than is necessary for decomposition of the metastable S phase layer. Well-established kinetic analysis also predicted similar outcomes;
- Femtosecond (fs) laser texturing within the KHz frequency range did not cause the decomposition of nitrogen supersaturated metastable S phase surfaces. This is largely due to the athermal nature of fs pulse laser texturing via rapid evaporation/ablation without appreciable heat diffusion;
- No discernible changes in chemical composition, cross-sectional layer structure and electrochemical corrosion properties could be found in the S phase following fs texturing. Hence, it is feasible to texture metastable S phase surfaces using fs lasers without causing undue deterioration of the S-phase layers.

Therefore, it is feasible to texture S phase surfaces using femtosecond pulsed lasers, thus paving the way towards long-lasting multi-functional antibacterial stainless steel surfaces.

6   Acknowledgements

7 <u>References</u>

[1] J.R. Davis, Stainless steels, ASM international, 1994.

[2] A. Dewangan, A. Patel, A. Bhadania, Stainless steel for dairy and food industry, Research Journal of Animal Husbandry and Dairy Science 6(1) (2015) 66-71.

[3] Y.P. Kathuria, An overview on laser microfabrication of bicompatible metallic stent for medical therapy, Laser-Assisted Micro-and Nanotechnologies 2003, International Society for Optics and Photonics, 2004, pp. 234-245.

[4] J. Verran, K. Whitehead, Factors affecting microbial adhesion to stainless steel and other materials used in medical devices, The International journal of artificial organs 28(11) (2005) 1138-1145.

[5] Y. Ren, K. Yang, B. Zhang, Y. Wang, Y. Liang, Nickel-free stainless steel for medical applications, Journal of Materials science and technology 20(5) (2004) 571-573.

[6] P. Decléty, Metals used in the food industry, Ecyclopaedia of Food Science, Food Technology and Nutrition (2003) 3869-3876.

[7] A.C.L. Wong, Biofilms in food processing environments, Journal of dairy science 81(10) (1998) 2765-2770.

[8] H. Kusumaningrum, G. Riboldi, W. Hazeleger, R. Beumer, Survival of foodborne pathogens on stainless steel surfaces and cross-contamination to foods, International journal of food microbiology 85(3) (2003) 227-236.

[9] R. Chmielewski, J. Frank, Biofilm formation and control in food processing facilities, Comprehensive reviews in food science and food safety 2(1) (2003) 22-32.

[10] H. Dong, S-phase surface engineering of Fe-Cr, Co-Cr and Ni-Cr alloys, International Materials Reviews 55(2) (2010) 65-98.

[11] E. Menthe, K.-T. Rie, Further investigation of the structure and properties of austenitic stainless steel after plasma nitriding, Surface and Coatings Technology 116 (1999) 199-204.

[12] J.A. Barish, J.M. Goddard, Anti-fouling surface modified stainless steel for food processing, Food and Bioproducts processing 91(4) (2013) 352-361.

[13] A. Bruzzone, H. Costa, P. Lonardo, D. Lucca, Advances in engineered surfaces for functional performance, CIRP annals 57(2) (2008) 750-769.

[14] A. Garcia-Giron, J.-M. Romano, Y. Liang, B. Dashtbozorg, H. Dong, P. Penchev, S. Dimov, Combined surface hardening and laser patterning approach for functionalising stainless steel surfaces, Applied Surface Science 439 (2018) 516-524.

[15] R. Jagdheesh, B. Pathiraj, E. Karatay, G. Romer, A. Huis in 't Veld, Laser-induced nanoscale superhydrophobic structures on metal surfaces, Langmuir 27(13) (2011) 8464-8469.

[16] J. Hasan, R.J. Crawford, E.P. Ivanova, Antibacterial surfaces: the quest for a new generation of biomaterials, Trends in biotechnology 31(5) (2013) 295-304.

[17] V.T. Pham, V.K. Truong, D.E. Mainwaring, Y. Guo, V.A. Baulin, M. Al Kobaisi, G. Gervinskas, S. Juodkazis, W.R. Zeng, P.P. Doran, Nanotopography as a trigger for the microscale, autogenous and passive lysis of erythrocytes, Journal of Materials Chemistry B 2(19) (2014) 2819-2826.

[18] J. Wahab, M.J. Ghazali, W.M.W. Yusoff, Z. Sajuri, Enhancing material performance through laser surface texturing: A review, Transactions of the IMF 94(4) (2016) 193-198.

[19] E. Roliński, Effect of plasma nitriding temperature on surface properties of austenitic stainless steel, Surface Engineering 3(1) (1987) 35-40.

[20] E.J. Mittemeijer, M.A. Somers, Thermochemical surface engineering of steels: improving materials performance, Elsevier, 2014.

[21] L. Gil, S. Brühl, L. Jimenez, O. Leon, R. Guevara, M.H. Staia, Corrosion performance of the plasma nitrided 316L stainless steel, Surface and Coatings Technology 201(7) (2006) 4424-4429.

[22] J. Buhagiar, 25 years of S-phase, Taylor & Francis, 2010.

[23] Y. Cao, F. Ernst, G. Michal, Colossal carbon supersaturation in austenitic stainless steels carburized at low temperature, Acta Materialia 51(14) (2003) 4171-4181.

[24] J. Buhagiar, T. Bell, R. Sammons, H. Dong, Evaluation of the biocompatibility of S-phase layers on medical grade austenitic stainless steels, Journal of Materials Science: Materials in Medicine 22(5) (2011) 1269-1278.

[25] X. Li, Y. Sun, T. Bell, The stability of the nitrogen S-phase in austenitic stainless steel, Zeitschrift fur Metallkunde(Germany) 90(11) (1999) 901-907.

[26] B. Brink, K. Ståhl, T.L. Christiansen, M.A. Somers, Thermal expansion and phase transformations of nitrogen-expanded austenite studied with in situ synchrotron X-ray diffraction, Journal of Applied Crystallography 47(3) (2014) 819-826.

[27] Y. Sun, X. Li, T. Bell, X-ray diffraction characterisation of low temperature plasma nitrided austenitic stainless steels, Journal of Materials Science 34(19) (1999) 4793-4802.

[28] T. Christiansen, M.A. Somers, On the crystallographic structure of S-phase, Scripta Materialia 50(1) (2004) 35-37.

[29] Y. Peng, Z. Liu, Y. Jiang, B. Wang, J. Gong, M.A. Somers, Experimental and numerical analysis of residual stress in carbon-stabilized expanded austenite, Scripta Materialia 157 (2018) 106-109.

[30] X. Li, S. Thaiwatthana, H. Dong, T. Bell, Thermal stability of carbon S phase in 316 stainless steel, Surface Engineering 18(6) (2002) 448-451.

[31] H. Mustafa, M. Mezera, D.T.A. Matthews, G. Römer, Effect of surface roughness on the ultrashort pulsed laser ablation fluence threshold of zinc and steel, Applied Surface Science 488 (2019) 10-21.

[32] Bodycote, Laser welding of s³p-treated components. [Online]. Accessed From: https://www.bodycote.com/wp-content/uploads/2018/12/Spotlight_S3P_LaserWelding_EN_02-S.pdf, (2018), [16/05/2019].

[33] S.C. Gallo, H. Dong, On the fundamental mechanisms of active screen plasma nitriding, Vacuum 84(2) (2009) 321-325.

[34] S. Sundaram, E. Mazur, Inducing and probing non-thermal transitions in semiconductors using femtosecond laser pulses, Nature materials 1(4) (2002) 217.

[35] A. Alshaer, B. Rogers, L. Li, Smoothed Particle Hydrodynamics (SPH) modelling of transient heat transfer in pulsed laser ablation of Al and associated free-surface problems, Computational Materials Science 127 (2017) 161-179.

[36] B.N. Chichkov, C. Momma, S. Nolte, F. Von Alvensleben, A. Tünnermann, Femtosecond, picosecond and nanosecond laser ablation of solids, Applied Physics A 63(2) (1996) 109-115.

[37] E. Williams, E. Brousseau, Nanosecond laser processing of Zr41. 2Ti13. 8Cu12. 5Ni10Be22. 5 with single pulses, Journal of Materials Processing Technology 232 (2016) 34-42.

[38] V.S. Saji, H.C. Choe, Electrochemical corrosion behaviour of nanotubular Ti–13Nb–13Zr alloy in Ringer's solution, Corrosion Science 51(8) (2009) 1658-1663.

[39] A.T. Tsubaki, M.A. Koten, M.J. Lucis, C. Zuhlke, N. Ianno, J.E. Shield, D.R. Alexander, Formation of aggregated nanoparticle spheres through femtosecond laser surface processing, Applied surface science 419 (2017) 778-787.

[40] D. Peng, T.-H. Kim, J.-H. Chung, J.-K. Park, Development of nitride-layer of AISI 304 austenitic stainless steel during high-temperature ammonia gas-nitriding, Applied Surface Science 256(24) (2010) 7522-7529.

[41] L. Mohan, C. Anandan, V.W. Grips, Investigation of electrochemical behavior of nitrogen implanted Ti–15Mo–3Nb–3Al alloy in Hank's solution, Journal of Materials Science: Materials in Medicine 24(3) (2013) 623-633.

[42] K. Fleischer, D. Caffrey, L. Farrell, E. Norton, D. Mullarkey, E. Arca, I.V. Shvets, Raman spectra of p-type transparent semiconducting Cr2O3: Mg, Thin Solid Films 594 (2015) 245-249.

[43] L. Bokobza, J.-L. Bruneel, M. Couzi, Raman spectroscopy as a tool for the analysis of carbon-based materials (highly oriented pyrolitic graphite, multilayer graphene and multiwall carbon nanotubes) and of some of their elastomeric composites, Vibrational Spectroscopy 74 (2014) 57-63.

[44] M. Knyazeva, M. Pohl, Duplex steels. Part II: carbides and nitrides, Metallography, Microstructure, and Analysis 2(5) (2013) 343-351.

[45] C.E. Butzke, Winemaking problems solved, Elsevier, 2010.

[46] J. Wang, Z. Li, D. Wang, S. Qiu, F. Ernst, Thermal stability of low-temperature-carburized austenitic stainless steel, Acta Materialia 128 (2017) 235-240.

[47] X. Yuan, Y. Zhao, X. Li, L. Chen, Effects of Gas Nitriding Temperature on the Surface Properties of a High Manganese TWIP Steel, Metals 7(3) (2017) 102.

[48] F. Bauer, A. Michalowski, T. Kiedrowski, S. Nolte, Heat accumulation in ultra-short pulsed scanning laser ablation of metals, Optics express 23(2) (2015) 1035-1043.

[49] T. Christiansen, M.A. Somers, Decomposition kinetics of expanded austenite with high nitrogen contents, Zeitschrift für Metallkunde 97(1) (2006) 79-88.

[50] T.L. Christiansen, M.A. Somers, Low-temperature gaseous surface hardening of stainless steel: the current status, International Journal of Materials Research 100(10) (2009) 1361-1377.

[51] D. Williamson, O. Ozturk, R. Wei, P.J. Wilbur, Metastable phase formation and enhanced diffusion in fcc alloys under high dose, high flux nitrogen implantation at high and low ion energies, Surface and Coatings Technology 65(1-3) (1994) 15-23.

[52] A. Bowen, G. Leak, Solute diffusion in alpha-and gamma-iron, Metallurgical Transactions 1(6) (1970) 1695-1700.

[53] Z.L. Zhang, T. Bell, Structure and Corrosion Resistance of Plasma Nitrided Stainless Steel, Surface Engineering 1(2) (1985) 131-136.

[54] S. Nolte, C. Momma, H. Jacobs, A. Tünnermann, B.N. Chichkov, B. Wellegehausen, H. Welling, Ablation of metals by ultrashort laser pulses, JOSA B 14(10) (1997) 2716-2722.

[55] R. Melchers, R. Jeffrey, Surface "Roughness" effect on marine immersion corrosion of mild steel, Corrosion 60(7) (2004) 697-703.